A computational multi-node electro-thermal model for large prismatic lithium-ion batteries

Shichun Yang[a], Yang Hua[a], Sida Zhou[a], Rong He[a], Yulong Zhang[a], Yu-wei Pan[a,*] , Xinhua Liu[a,**], Yubo Lian[c],Billy Wu[b]

[a] School of Transportation Science and Engineering, Beihang University, Beijing, China

[b] Dyson School of Design Engineering, Imperial College, London, UK

[c] BYD Auto Industry Co., Ltd., Shenzhen, 518118, China

*Corresponding author: knell94@buaa.edu.cn (Yu-Wei Pan)

**Corresponding author: liuxinhua19@buaa.edu.cn (Xinhua Liu)

Highlight

1. A pseudo 3D coupled multi-node electro-thermal model for online temperature prediction with excellent precision is presented.

2. Detailed internal geometric structure of the cell is simulated without increasing node numbers.

3. High accuracy online temperature estimation under a wide operation range when matching the experimental data or comparing with a finite-element model.

Abstract

During operation of large form factor prismatic lithium-ion batteries, temperature heterogeneities are aggravated which affect the performance, lifetime and safety of the cells and packs. Therefore, an accurate model to predict the evolution of temperature profiles in a cell is essential for effective thermal management. In this paper, a pseudo 3D coupled multi-node electro-thermal model is presented for real-time prediction of the temperature field evolution on the surface and inside the

battery. The model consists of two parts to investigate the heterogeneous temperature distribution during the battery operation: a heat generation model based on a second order equivalent-circuit model and a multi-node heat transfer model based on the battery geometry. Three types of nodes are adopted to describe the thermal characteristics of various components of the cell. Simulation results show that the proposed model has a great consistency with a finite element method, and its computational cost is significantly reduced. The validity of the coupled electrical and thermal model is also demonstrated experimentally for a 105 Ah prismatic cell applying wide ranges of temperature and SOC. The maximum error is less than 2 K and the RMSE is less than 1 K throughout the cycles. The proposed model holds a great potential for online temperature estimation in advanced lithium-ion battery thermal management system design.

Graphic abstract

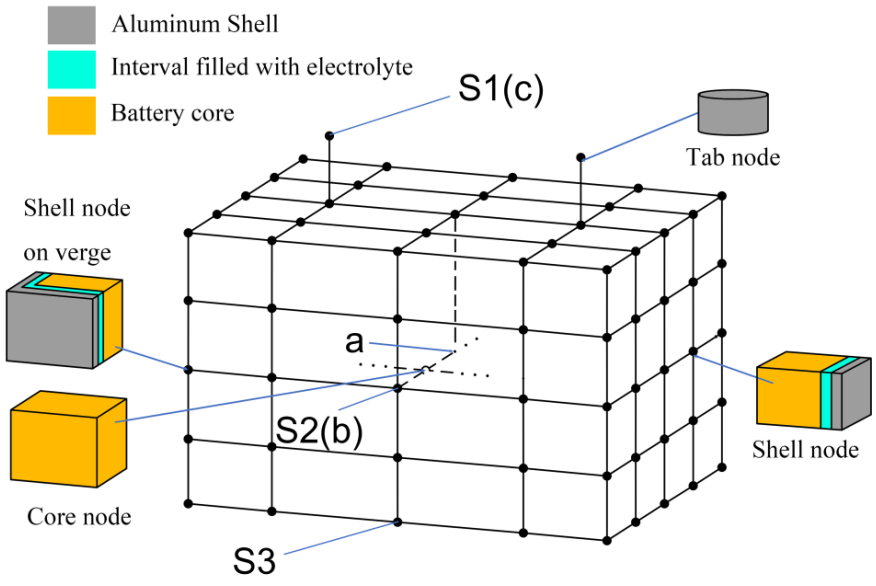

1. Introduction

Electric vehicles (EVs) and hybrid electric vehicles (HEVs) are essential technologies to

resolve the energy crisis and prevent severe environmental problems [1-3]. Lithium-ion batteries (LIBs), with their relatively high energy density and long cycle life, have been extensively commercialized as energy storage technologies for EVs and HEVs over other types of batteries [1]. Generally, there are three form factors of LIB cells: pouch, cylindrical and prismatic. Among these, the prismatic type has become an attractive solution for EVs due to their high packing density and relative ease of manufacturing through the application of a jelly roll design [8].

The durability and reliability of LIBs are greatly affected by operating temperature [4]. Reduced ionic conductivity at low temperatures limits the performance, and results in large voltage polarization as well as slow solid-state diffusion which in anodes can lead to lithium plating [12,16] and consequentially limited lifetime was well as safety concerns. High operating temperatures results in faster parasitic side reactions and can significantly accelerate the degradation of the cells or even cause thermal runaway [6,7,23]. Temperature heterogeneity in large form factor cells can lead to uneven current density distributions, local SOC differences and local aging differences, which may also accelerate the global aging of the battery [5]. Current trends in LIB design have seen many large capacity cells factor the prismatic form factor, which whilst simplifying the pack design by reducing the number of parallel connections results in more severe temperature heterogeneities in cells due to the uneven ability of the cell to remove heat from central regions. Therefore, it is important to be able to predict and control the temperature of the cell within an ideal range to promote temperature uniformity by developing effective and accurate battery thermal management systems (BTMS) [6].

In order to achieve an effective BTMS, an accurate prediction of the battery pack temperature profile is essential. In most cases, however, it is difficult to monitor the temperature distribution inside the cell or the battery pack with sensors. Therefore, a precise thermal model is crucial for BTMS. Generally, a battery thermal model consists of two parts: a heat generation model and a heat transfer model.

Heat generation models can be roughly classified into three categories: physics-based electrochemical models [1,2,9,17], black-box empirical models [10,19,20] and equivalent circuit models (ECM) [8,11,12]. The black-box empirical model is usually based on

experimentally measured rates of heat generation and relies on empirical equations or other fitting strategies to acquire the heat generation under different working conditions. The precision of the black-box empirical models, however, is usually limited to certain cases [18,19] with limited insights into internal temperature distributions. Electrochemical models based on porous electrode and concentrated solution theory [13,22] can achieve high accuracy if all the parameters are calibrated carefully and sufficient computational resources are provided. However, such models are usually too computationally expensive to be applied in a battery management system (BMS) or BTMS. The ECM can reach adequate precision while having an acceptable computational cost and has been broadly applied in real-time battery parameter estimation [27,34] and modelling of the heat generation rate in cells [21]. To better describe the heat sources in a LIB, an ECM is usually combined with the general energy balance equation proposed by Bernardi et al. [24]. This includes both reversible and irreversible heat, and thus can capture the heat generation rate of the cells under most working conditions.

The heat transfer model is another important component of a battery thermal system. Various works have focused on developing models which describe the temperature rise or the internal temperature profile of LIBs. One of these approaches is based on using Finite Element Analysis (FEA) [3-8,28]. FEA based approaches can usually reach a very high accuracy, but the heavy computational cost greatly limits its real-time application. Alternative solutions to model the temperature profile of LIBs are the lumped multi-node [9,10,12,13,25,26] or heat capacitor-resistance models [8] based on the analogy between thermal and electrical phenomena [14]. Usually, a lumped multi-node model assumes all parameters to be uniform and irrelevant to the location of the nodes [11]. Both lumped multi-node models or heat capacitor-resistance models usually ignore the detailed internal structure of the battery. Some literatures [30,31], however, have shown that the geometry of LIB, such as tab position or thickness of the metal foils, may have significant influence on the overall heat transference of the cell.

The parameterization procedure also plays an important role in deciding the accuracy of models. For electrical parameters, including resistances and capacitors, several fitting strategies have already been proposed [21,29,30]. The method to obtain thermal properties of

the cell is relatively more complicated. For instance, the anisotropic heat transference coefficient is difficult to ascertain without disassembling the battery [32,33].

To better characterize the temperature gradient inside large prismatic LIBs, this paper presents a pseudo 3D multi-node electrical-thermal model (MNETM) to describe the shell-interval-core structure of a LIB. The electrical parameters are fitted by the particle-swarm algorithm with pulse discharge experiments under different ambient temperatures, and the thermal properties are either fitted, provided by the battery supplier or cited from literature. Experimental results show that the model can accurately capture the temperature evolution of the battery under various operating conditions. The comparison with a FEA model verifies that the MNETM can estimate the temperature gradient inside the cell at high precision with little computational cost.

The rest of the paper is organized as follows: Section 2 describes the coupled electrical-thermal model, and its two sub-models are introduced. Section 3 explains the multiple experimental cycles applied in the study. In Section 4, a comparison between the MNETM, experimental data and a finite-element model is presented. Finally, section 5 concludes the paper, and the future works are presented.

2. Model development

In this section, the coupled MNETM is established. Utilizing only current as the input, the model can predict the internal temperature distribution and the SOC of the battery. As discussed above, the model consists two sub-models: a heat generation model based on a second order ECM and a battery geometry based multi-node heat transfer model. Firstly, the irreversible heat is estimated by the ECM, and the reversible heat is calculated based on the input current and the cell's SOC. Further, the heat generated by the cell is distributed to all nodes based on the volume, from which the temperature distribution is calculated. As the electrochemical process of a LIB is very sensitive to the temperature, the average temperature of all electrochemically active nodes are fed back to the ECM to determine the model's parameters. A schematic illustration of the model can be found in Fig. 1.

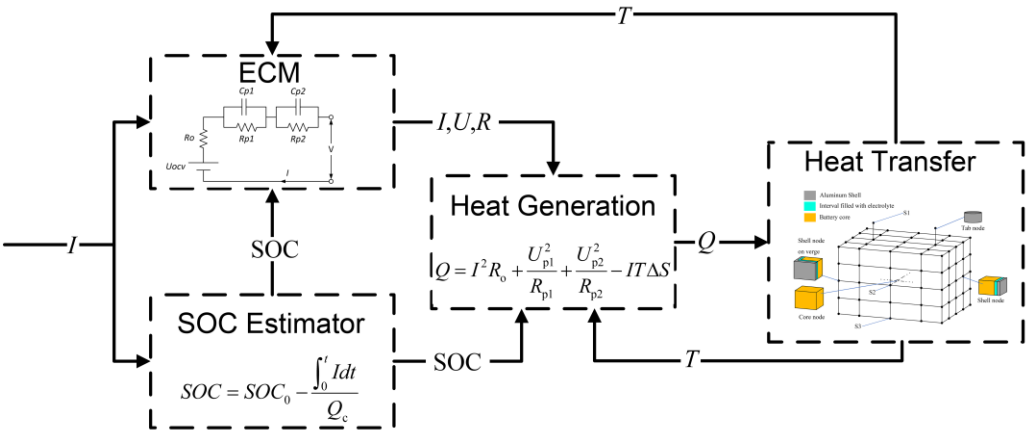

Fig. 1 Schematic illustration of the MNETM

2.1. Heat generation model

As shown in Eq. 1, the total heat generated during the operation of a LIB can be divided into two parts: irreversible heat and reversible heat.

$$\dot{Q} = \dot{Q}_{irr} + \dot{Q}_{rev} \tag{1}$$

The irreversible heat is caused by multiple sources such as Ohmic losses due to electron/ionic transport or the overpotential of the electrochemical reaction, with this always being positive. The reversible heat, however, is related to the entropy change associated with electrochemically driven phase changes in the electrode materials, and the sign of it varies with the cell's SOC and the current direction. In this paper, the irreversible heat is calculated as the energy loss of the ECM and the reversible heat is estimated based on the current, temperature and entropic coefficient of the cell.

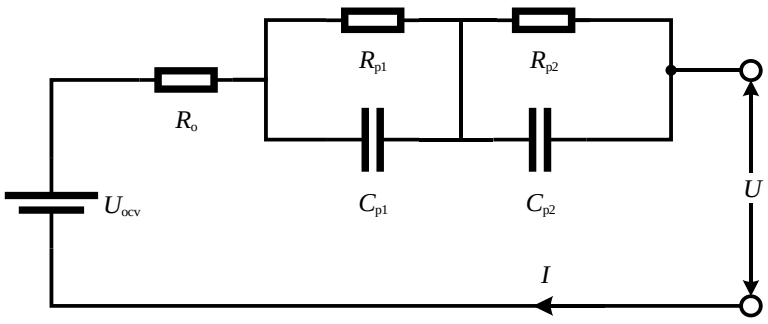

Fig. 2 Second-order equivalent-circuit model

As the ECM of the LIB can estimate the voltage loss of the cell with low computational cost, it is one of the ideal tools to achieve online prediction of the irreversible heat. The

second-order ECM applied in this paper is shown in Fig. 2, where R_o represents the Ohmic resistance of the cell and the two RC components represents the polarization resistance with different time constants. The state-space equations of the model can be written as:

$$\begin{cases} U_o = IR_o \\ \dfrac{dU_{p1}}{dt} = \left(I - \dfrac{U_{p1}}{R_{p1}} \right) \dfrac{1}{C_{p1}} \\ \dfrac{dU_{p2}}{dt} = \left(I - \dfrac{U_{p2}}{R_{p2}} \right) \dfrac{1}{C_{p2}} \\ U = U_{OCV} - U_{p1} - U_{p2} - U_o \end{cases} \tag{2}$$

where U_{ocv} is the open-circuit voltage of the cell, I is the current, U_{p1} and U_{p2} are the polarization voltage, R_{p1} and R_{p2} are the polarization resistances, C_{p1} and C_{p2} are the polarization capacitors.

Under the relaxation period where current equals 0 A, an analytical solution can be derived from the differential equations in Eq. 3:

$$U_p(t) = U_{p,0} \exp\left(-\frac{t}{\tau} \right) \tag{3}$$

where $U_{p,0}$ is the polarization voltage at the beginning of the relaxation period. $\tau = R_p C_p$ is called time constant.

The irreversible heat can be calculated as:

$$\dot{Q}_{irr} = I^2 R_o + \frac{U_{p1}^2}{R_{p1}} + \frac{U_{p2}^2}{R_{p2}} \tag{4}$$

In this paper, the R/C-SOC relationship is fitted at 273 K, 298 K and 318 K based on the voltage responses of the cell under pulse discharge experiments and by applying the particle swarm optimization (PSO) algorithm. The PSO algorithm begins with random particles representing position and velocity, and then generalizes all particles to the global optimal solution of the problem. Eq. 5 and Eq. 6 show the updating process of particle velocity and position.

$$\mathbf{v}_t = k\left[\mathbf{v}_{t-1} + c_1 \left(\mathbf{Pb}_{self} - \mathbf{P}_{t-1} \right) + c_2 \left(\mathbf{Pb}_{global} - \mathbf{P}_{t-1} \right) \right] \tag{5}$$

$$\mathbf{P}_t = \mathbf{P}_{t-1} + \mathbf{v}_t \tag{6}$$

where k is the attenuation factor; $\mathbf{v}$ is the speed vector; c_1 and c_2 are the acceleration factors,

respectively determining the influence of the individual-best position and global-best position; **Pb** is the best position of the particle and $\mathbf{P}_t$ is the current position.

The process of the PSO can be summarized as Table 1.

Table 1 Process of particle swarm optimization

Step 1: Initialize particles in the searching area with random position and velocity.
Step 2: Search for the individual-best and group-best optimal solution in all particles.
Step 3: Update the velocity and position of the particles based on Eq. 5 and Eq. 6.
Step 4: Iterate step 2 and step 3 until meeting the convergence requirement or reaching the maximum number of iterations.

U_{ocv}, however, does not affect the heat generation rate and therefore is calculated using the voltage at the end of the resting steps in the experiments.

Since the battery parameters, such as the Ohmic resistant, are strongly dependent with SOC, we divided the SOC range of the cell into 10 parts, and 11 sets of parameters are identified for the boundary of each area.

During simulation, the SOC of the cell is calculated based on Ampere hour integration, and the real-time value of the parameters are calculated using linear interpolation.

Following Bernardi et. Al [24], the reversible heat can be written as:

$$\dot{Q}_{\text{rev}} = -\sum I_i T \frac{dU_i}{dT} \tag{7}$$

where I_i and U_i are the current and equilibrium potential of the i^{th} species, which represents the negative and positive electrode of the battery.

Although various methods have been proposed to obtain the value of the cathode and anode entropy coefficient through experiments, these methods usually require disassembling the cell and the precision is strongly affected by the relaxation effect. Therefore, as the absolute value of current flow in cathode and anode is nearly the same, $\mathrm{d}U_i/\mathrm{d}T$ is integrated to a single parameter ΔS and is fitted based on the temperature change of the cell under 318 K, 1.5 C discharging. Therefore, the reversible heat in this study follows Eq. 8.

$$\dot{Q}_{\text{rev}} = -IT\Delta S \tag{8}$$

It should also be noted that during the operation of a LIB, energy loss caused by the contact resistance of the cell's tab may generate large amount of heat. In this work, the

terminal resistance is assumed to be independent with temperature or current, and the heat generation rate of the tabs is described as:

$$\dot{Q}_{\text{tab}} = I^2 R_{\text{tab}} \tag{9}$$

where R_{tab} is the terminal resistance.

2.2. Heat transfer model

Due to their low computational cost, multi-node thermal models have been widely adopted to estimate the temperature of lithium-ion cells or packs in real-time, but these models usually ignore the detailed geometry of the cell [5].

In this section, a multi-node thermal model is proposed, and three types of nodes are implemented to capture the thermal properties of different components of the cell. These include: core nodes, terminal nodes (tab node) and shell/verge/corner nodes. To reduce the complexity of the battery geometry, the following assumptions are proposed: 1) As the scale of the current collector-electrodes-separator structure is much smaller than the whole battery, the battery core is treated as a homogenous solid cube with anisotropic thermal conductivity. 2) The heat generation heterogeneity caused by the temperature gradient across the core is ignored, thus the heat generated is distributed to each node based only on the battery core volume contained in each node. 3) Thermal parameters (including heat transfer coefficient and specific heat capacity) are assumed to be independent of temperature. 4) Heat transfer inside the cell due to convection and all heat transfer due to radiation are ignored.

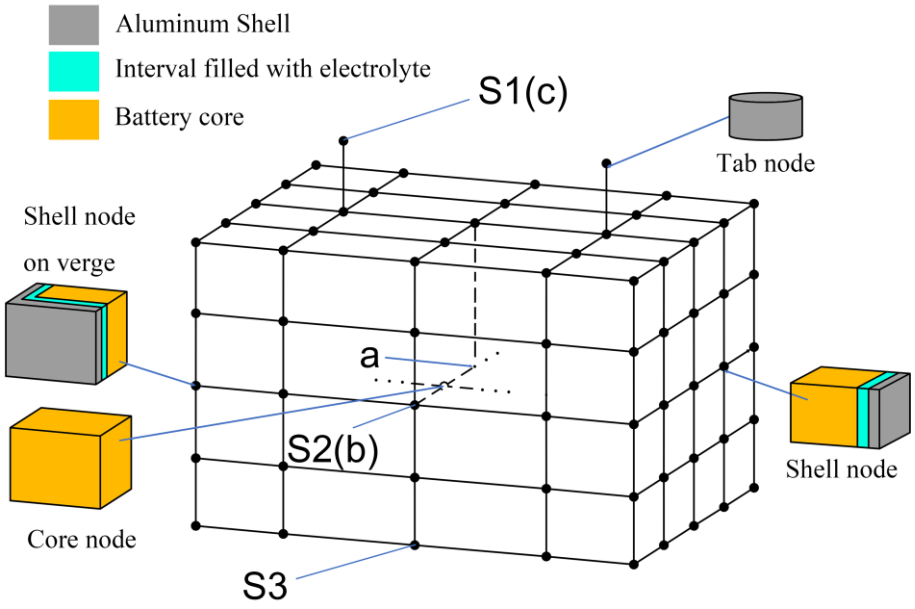

Fig. 3 Multi-node heat transference model and the three types of node

Considering the above assumptions, the definition of the three types of nodes, specifically the core node, terminal node and shell node, are shown in Fig. 3.

The core nodes consist of the electrodes, current collectors and separators. Due to the thermal properties of these components and the thermal contact resistances, the in-plane (directions that parallels with *y*-*z* plane in Fig. 3) and through-plane (perpendicular to *y*-*z* plane) thermal conductivity differs significantly. As shown in Fig. 3, each core node is thermally connected to its 6 neighboring nodes, and the heat transference function of the core node located at point (*i*, *j*, *k*) can be written as:

$$\begin{aligned} m_{i,j,k}C\dot{T}_{i,j,k} = \dot{Q}_{i,j,k} &+ \frac{S_{j,k}h_x\left(T_{i+1,j,k}-T_{i,j,k}\right)}{l_{i,i+1}} + \frac{S_{j,k}h_x\left(T_{i-1,j,k}-T_{i,j,k}\right)}{l_{i,i-1}} \\ &+ \frac{S_{i,k}h_y\left(T_{i,j+1,k}-T_{i,j,k}\right)}{l_{j,j+1}} + \frac{S_{i,k}h_y\left(T_{i,j-1,k}-T_{i,j,k}\right)}{l_{j,j-1}} \\ &+ \frac{S_{i,j}h_z\left(T_{i,j,k+1}-T_{i,j,k}\right)}{l_{k,k+1}} + \frac{S_{i,j}h_z\left(T_{i,j,k-1}-T_{i,j,k}\right)}{l_{k,k-1}} \end{aligned} \tag{10}$$

where *m* is the mass of the node, *C* is the specific heat capacity of the node, which is assumed to be uniform across the cell, *l* and *S* are the distance and contact area between the two neighboring nodes respectively.

In this paper, two terminal nodes are established to capture the heat generation and heat

exchange of the tabs. The heat transfer characteristics of the terminal nodes are described as:

$$m_{\text{tab}} C_{\text{tab}} \dot{T}_{\text{tab}} = \dot{Q}_{\text{tab}} + \frac{S_{\text{c, tab}} h_{\text{tab}} \left(T_{\text{sh}} - T_{\text{tab}} \right)}{l_{\text{tab,sh}}} + h S_{\text{s,tab}} \left(T_{\text{amb}} - T_{\text{tab}} \right) \tag{11}$$

where the subscript sh represents the corresponding shell node connecting to the tab, $S_{\text{c,tab}}$ is the contact surface between the tab node and the shell node, $S_{\text{s,tab}}$ is the surface area of the tab.

Under the above description, two shell nodes need to be directly placed under the terminal node, and a node located at the center of the cell is needed to capture the core temperature, therefore, the least node numbers on *x*, *y*, *z* direction are 3, 5, 3 respectively.

Comparing to the above two types of nodes, the shell nodes have a relatively complex structure. Due to the scale difference between the shell, interval and the battery core, the shell and the interval are not modeled directly, but represented by an integrated shell node. Therefore, most shell nodes contain multiple layers in one direction and its in-plane (direction parallel to the shell) and through-plane (direction vertical to the shell) properties can be calculated as Eq. 12 and Eq. 13 respectively.

$$h_{\parallel} = \frac{S_{\text{sh}} h_{\text{sh}} + S_{\text{int}} h_{\text{int}} + S_{\text{core}} h_{\text{core}}}{S_{\text{sh}} + S_{\text{int}} + S_{\text{core}}} \tag{12}$$

$$h_{\perp} = \frac{l_{\text{sh}} + l_{\text{int}} + l_{\text{core}}}{\frac{l_{\text{sh}}}{h_{\text{sh}}} + \frac{l_{\text{int}}}{h_{\text{int}}} + \frac{l_{\text{core}}}{h_{\text{core}}}} \tag{13}$$

At the bottom of the cell, there is an insulation material and a contact resistance, but the method to calculate total heat transfer coefficient remains the same.

As the terminals are electrically connected with the battery core with current collectors, the heat transference of nodes under the terminals also needs to be modified. As the current collectors of LIBs are usually very thin, it is reasonable to assume that this connection has limited influence on the in-plane heat exchange. For the in-plane heat transfer, the electrolyte can be considered in parallel with the current collectors. As the heat transfer coefficient of the electrolyte is much smaller than that of current collectors, the heat exchange through the electrolyte can be ignored. Furthermore, we also assumed that a terminal is only connected to a single node. Under the above simplification, the total heat exchange coefficients of the two nodes can still be calculated and applied, but both thermal and geometric properties of this

electrical connection are unknown and need to be fitted.

Nodes on the edge of the cell have a multi-layer structure in more than one direction, but these nodes can be split. Eq. 12 and Eq. 13 can be applied to each slice separately, and the total heat exchange coefficient can be calculated by integrating the slices with the same method.

The heat transference function of shell nodes can thus be written as:

$$m_{\mathrm{sh}} C \dot{T}_{\mathrm{sh}} = \dot{Q}_{\mathrm{sh}} + hS\left(T_{\mathrm{amb}} - T_{\mathrm{sh}}\right) + q \tag{14}$$

where q represents the heat transfer between the shell node and its neighboring nodes and can be calculated similarly to Eq. 10, and h and S are the heat transfer coefficient and surface area between the shell node and the ambient environment respectively.

Reorganizing Eq. 10 to Eq. 14, a state-space representation can be derived as:

$$\dot{\mathbf{T}} = \mathbf{D}\dot{Q} + \mathbf{H}\mathbf{T} \tag{15}$$

where **H** is the heat transfer matrix, **T** is the temperature matrix with a structure of Eq. 14.

$$\dot{\mathbf{T}} = \begin{bmatrix} \ldots & T_t & \ldots & T_{\mathrm{amb}} & T_{\mathrm{tab1}} & T_{\mathrm{tab2}} \end{bmatrix}^{\mathrm{T}} \tag{16}$$

The subscript t for the temperature of node (i, j, k) equals to (i-1)$N_{\mathrm{y}}N_{\mathrm{z}}$+($j$-1)$N_{\mathrm{z}}$+$k$, where N_{y} and N_{z} are the node numbers in the y and z direction, respectively.

D is the heat generation distribution matrix with a structure of Eq. 17.

$$\dot{\mathbf{D}} = \begin{bmatrix} \ldots & \dfrac{V_t}{V} & \ldots & 0 & \dfrac{\dot{Q}_{\mathrm{tab}}}{\dot{Q}} & \dfrac{\dot{Q}_{\mathrm{tab}}}{\dot{Q}} \end{bmatrix}^{\mathrm{T}} \tag{17}$$

where V_{t} is the battery core volume contained by the t^{th} node and V is the total volume of the battery core.

Note that although a high-dimensional matrix will be formed with the increase of the total node number, a node can have at most 6 neighbors, therefore, the time and space complexity can both be optimized to be linear with the total number of nodes.

2.3. 3D FEA electro-thermal model

In this section, a 3D FEA thermal model is established in COMSOL Multi-physics to

verify the ability of the MNETM to capture the battery core temperature. As the boundary conditions are symmetrical in both the x and y direction, the FEA model can be simplified to a 1/4 battery model, as shown in Fig. 4. The FEA model shares the same thermal and electrical properties with the MNETM and is expected to have a similar temperature output as the pseudo 3D multi-node model.

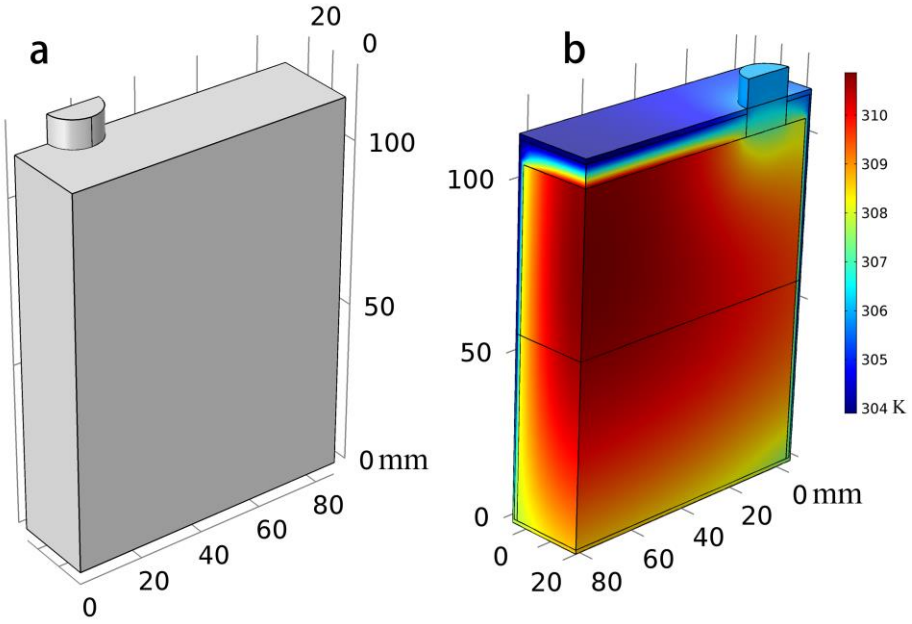

Fig. 4 Battery FEA model: (A) Model geometry. (B) Temperature distribution at the end of the 1.5C constant current discharging cycle under 298K

3. Experimental

All experiments were carried out with a 105 Ah prismatic lithium-ion battery which has an NCM based cathode and a graphite anode. The specification and properties of the cell are given in Table 2. To parameterise and validate the combined model and its sub-models, three experimental setups are implemented.

Table 2 Model Parameters

Parameters	Value	Unit
Rated Capacity	105^{p}	Ah
Nominal Voltage	3.6^{p}	V

Discharge Cut-off Voltage	2.5[p]	V
Charge Cut-off Voltage	4.2[p]	V
Height (z direction)	114[p]	mm
Width (x direction)	50[p]	mm
Length (y direction)	173[p]	mm
h_x	1.696[p]	W/ (m K)
h_y	29.94[p]	W/ (m K)
h_z	29.94[p]	W/ (m K)
h_{air}, environmental chamber	84.82[f]	W/ (m^2 K)
h_{air}, natural cooling	9.36[f]	W/ (m^2 K)
$h_{aluminum}$	237	W/ (m K)
$h_{electrolyte}$	0.172[35]	W/ (m K)
$h_{cooling—plate}$	141[f]	W/ (m K)
Thermal conductivity of tab-core connection	0.0095[f]	W m / K
Thermal resistance, bottom	0.0017[f]	m^2 K / W
R_{tab}	7.48e-5[f]	Ω
R_{ohm} (298K, 0.5 SOC)	6.1e-4[f]	Ω
R_{p1} (298K, 0.5 SOC)	3.1e-4[f]	Ω
R_{p2} (298K, 0.5 SOC)	2.4e-4[f]	Ω
τ_1 (298K, 0.5 SOC)	40.3[f]	s
τ_2 (298K, 0.5 SOC)	828[f]	s
Interval in *x* direction	1.2[p]	mm
Interval in *y* direction	1.2[p]	mm
Interval, top	6.7[p]	mm
Interval, bottom	6.7[f]	mm
Shell thickness, *x*	0.6[p]	mm
Shell thickness, *y*	0.55[p]	mm
Shell thickness, bottom	1.2[p]	mm

Shell thickness, top	1.5[p]	mm

[f] fitted

[s] provided by battery supplier

In the first experiment, pulse discharge cycles at 273 K, 298 K, and 318 K were performed with a Neware battery cycler, Neware battery electronic load and a Sanxin environmental chamber. In each cycle, the cell was first charged using a constant current-constant voltage (CC-CV) step to the cut-off voltage of 4.2V under room temperature with the battery cycler. After the charging step, the battery was put into the chamber and rested for 3 hours. Then, the battery was discharged under a pulse discharging procedure with the electronic load, with each pulse using a current of 1 C (105 A) for 360 seconds. As the time of each pulse was short enough, no significant temperature rise was monitored. The detailed current and voltage profile of the experiment and the simulation result under 318 K is shown in Fig. 5.

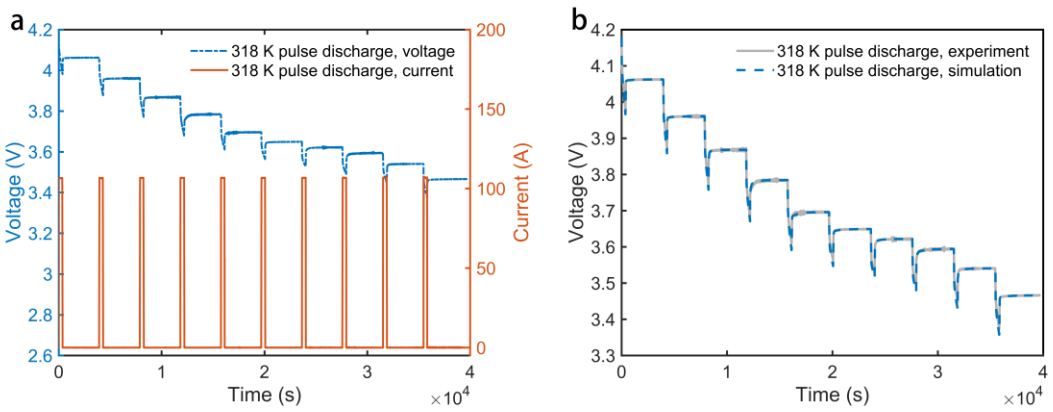

Fig. 5 Result of the pulse discharging cycle under 318K. (A) Cycle current and voltage profile. (B) Comparison between simulation and experimental result.

In the second test, the battery was discharged under different constant current and ambient temperatures in the environmental chamber to parameterize and validate the thermal model under air cooling conditions. To verify the model under different ambient temperatures, the 1.5 C discharging tests were carried out with an ambient temperature of 273 K, 298 K and 318 K. The convective heat transfer coefficient and the entropy coefficient were fitted under 298 K, and the data under 273 K and 318 K are for the validation of the model. After that, a 2 C discharge was performed at 318 K to test the performance of the model under different cycling rates. Under air-cooling condition, only one temperature sensor was placed on

position s2 in Fig. 3.

The third experiment performed was to test the model's ability to capture the thermal behaviour of the cell under non-uniform cooling condition and dynamic l current loads. In this experiment, the cell was cycled under a dynamic cycle derived from FTP-75 cycle with a water-cooling plate to replicate the operation condition of the batteries of an EV with water cooling system. The cooling plate worked below the cell and was in direct contact with the bottom of the battery. Three temperature sensors, located at position s1, s2 and s3 in Fig. 3 respectively were used to monitor the surface temperature profile of the cell.

4. Results and Discussion

4.1. Model validation under air cooling and constant current

The comparison between the simulation results (lines) and the experimental data (dots) under different ambient temperature and C-rate are shown in Fig. 6A and Fig. 6B respectively. It can be seen in Fig. 6B that the thermal behaviour of the cell is well captured under the fitting cycle (318 K, 1.5 C discharge and 318 K, 2 C discharge) and an adequate precision is achieved under the validation cycles in Fig. 6A. The maximum deviation between the simulation and experimental data is less than 2 K, and the RMSE under each cycle is less than 1 K, detailed information of the error is listed in Table 3.

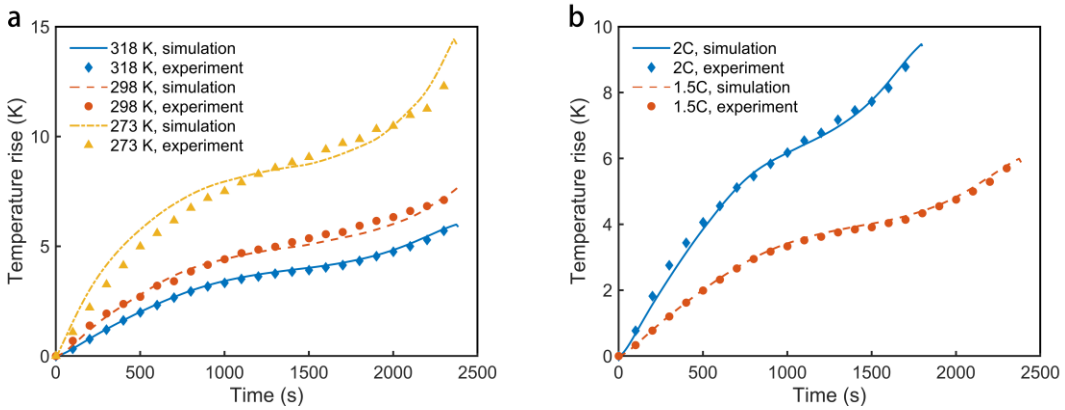

Fig. 6 Results of the constant discharging tests. (A) The comparison of simulated temperature increase and experimental data under different ambient temperature. (B) The comparison of simulated temperature rise and experimental data under different C-rate.

Table 3 RMSE and maximum error under constant discharging cycles

Cycle	RMSE (K)	Maximum error (K)
273 K, 1.5 C	0.8136	1.9648
298 K, 1.5 C	0.1727	0.5895
318 K, 1.5 C	0.0772	0.2166
318 K, 2 C	0.2218	0.5897

It should be noted that while the ambient temperature of the environment chamber can fluctuate to under 273 K, the temperature sensor cannot obtain data under 273 K. These invalid data are fitted linearly using the neighbouring points.

4.2. Model validation under water cooling and dynamic driving cycle

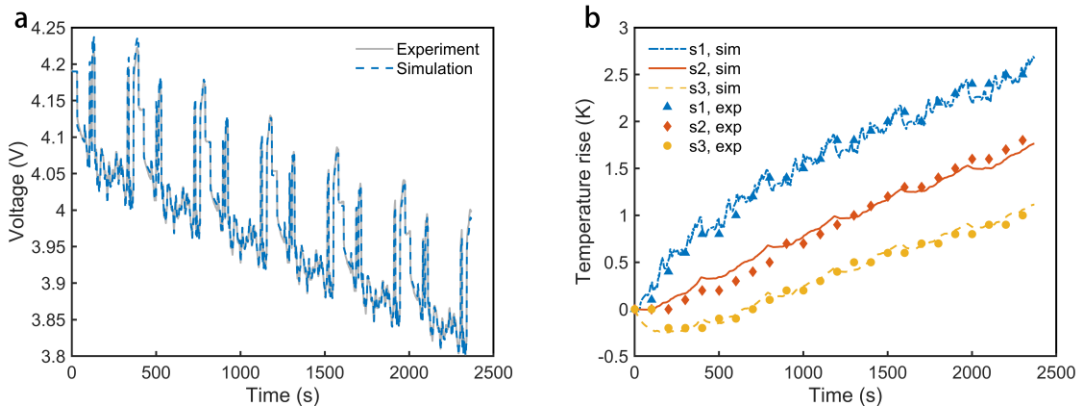

Fig. 7 Results of the water-cooling dynamic cycle. (A) Voltage profile of the cycle. (B) Simulated and real temperature rise at the three temperature sensors.

The result of the water-cooling test is presented in Fig. 7. The driving cycle applied under water cooling is derived from the FTP-75 cycle but is slightly modified to suit the capability of the battery cycler. The voltage profile of the cycle is shown in Fig. 7A. It can be found the model output is in excellent agreement with the experimental data, which guarantees the accuracy of the estimated irreversible heat.

The temperature rise during the cycle is presented in Fig. 7B, where sensor 1 (s1), sensor 2 (s2) and sensor 3 (s3) are located at the left terminal, center of the front surface and bottom of the front surface respectively, and the estimation errors of temperature and voltage are shown in Table 4.

As the terminal is the furthest point from the cooling plate and is heated by the terminal

contact electrical resistance, s1 maintained the highest temperature. It can also be observed that the terminal temperature responds much quicker to the current change than the two other sensors, which indicates that the terminal temperature may not be a good indicator of the cell's internal temperature under large current fluctuation.

The temperature of the cooling water is around 1 K lower than the ambient temperature, thus the temperature of sensor 3 first experienced a drop at the beginning of the cycle. After 500 second, the temperature at s3 begin to rise but keeps being the lowest over the entire cycle.

Table 4 Error under dynamic cycling

	RMSE	Maximum error
Sensor 1, temperature (K)	0.4579	0.7946
Sensor 2, temperature (K)	0.1087	0.2586
Sensor 3, temperature (K)	0.1134	0.2828
Voltage (V)	0.0113	0.0818

4.3. Model validation compared with finite element model

The temperature evolution of point a (geometric center), b (front surface center), c (center of the terminal top surface) and the corresponding node in the MNETM during the cycle is shown in Fig. 8. Fig. 8A illustrates the comparison between the FEA model and MNETM with the least node numbers on each direction. It can be found that while the accuracy at point a and point c is acceptable, the front temperature of MNETM is significantly larger that the FEA model. In the MNETM, the heat sources are simplified to be exactly located on each node, but these heat sources are separated from the surface node by an interval layer with low thermal conductivity, which leads to a higher surface temperature at point b. This deviation in temperature can further cause differences in the heat flux between the battery and the environment and finally brings a lower core temperature. The result of MNETM with larger node population is plot in Fig 7B. This increase in node number significantly reduced the error at point b and it can be expected that the error will be further reduced. when the node population is large enough.

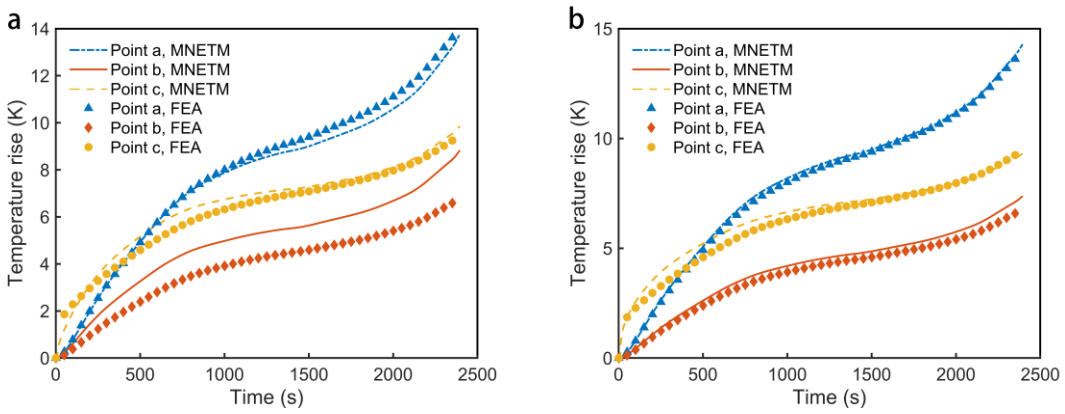

Fig. 8 Comparison between FEA model and MNETM with different node numbers. (A) MNETM with a node number of 3, 5, 3 on *x*, *y*, *z* direction. (B) MNETM with a node number of 7, 7, 5

Table 5 further compares the RMSE and computational time of MNETM with different numbers of nodes or without specific battery structure, where the MNETM without shell and without interval both have a node number of 5, 5, 5. The results of MNETM without certain structure of the cell indicates that both the aluminum case and the interval between the shell and battery core can strongly influence the heat flux of the cell. With the increased number of node points, the MNETM can reach a higher precision at point b and point c, but the error of temperature at the geometric center begin to rise when the node population increased from 125 to 245. The tested MNETM with the largest node population is still more than 10 times faster than the FEA model with only 1/4 geometry and a relatively larger sampling time.

Table 5 Comparison between FEA model and MNETM

Model type	RMSE (K)		Computing time (s)	Sampling time (s)
	Geometric center	Front surface center		
FEA model	-	-	94	1~20
MNETM, node number 3,5,3	0.3126	1.0810	6.204	1
MNETM, node number 5,5,5	0.0905	0.5097	7.525	1
MNETM, node number 7,7,5	0.1349	0.2880	7.795	1
MNETM without metal shell	1.500	0.9053	7.438	1
MNETM without interval	1.0584	1.2468	7.308	1

5. Conclusions

In this paper, a novel electro-thermal coupled model is presented to predict the temperature field evolution for prismatic LIBs. The model consists of two sub-models: an ECM heat generation model and a pseudo 3D multi-node heat transfer model. The model highlights the ability for online temperature prediction with excellent precision and high accuracy under wide operation range. Simulation results show that the MNETM has a great consistency with the finite element model, and the shell-interval-core nodes structure can significantly reduce the demand of computational resources. The effectiveness of the MNETM is also verified by real experimental tests under wide range of temperature and SOC. The maximum error is less than 2 K and the RMSE is less than 1 K throughout the cycles. Future efforts will focus on extending the MNETM model to battery packs with complex cooling boundaries and finally integrate it into the existing LIB TMSs.

Nomenclature

Symbols

Q	Heat generation in J or Quantity of electric charge in Coulomb
U	Voltage in V
I	Current in A
R	Resistance in Ω
C	Capacitor in F or specific heat capacity in J/ (kg K)
t	Time in s
τ	Time constant in s
T	Temperature in K
m	Mass in kg
l	Distance in m
h	Heat transfer coefficient in W / (m^2 K)
$\mathbf{H}$	heat transfer matrix

D	Heat generation distribution matrix
S	Surface area in m^2
ΔS	Entropy change in V/K
RMSE	Root Mean Squared Error
V	Volume in m^3
q	heat exchange in W

Subscripts

irr	irreversible
i	species or battery components
rev	reversible
p	polarization
ocv	open-circuit voltage
o	ohmic
p	positive
n	negative
tab	Battery tab
int	interval between the shell and the battery core
sh	shell node
core	battery core
amb	ambient environment

Acknowledge

This work is supported by the National Key Research and Development Program of China (2018YFB0104400), and National Science Foundation of China (No.U1864213) .

References

[1] Sun F, Xiong R, He H, et al. Model-based dynamic multi-parameter method for peak power estimation of lithium–ion batteries[J]. Applied Energy, 2012,96:378-386.

[2] Lu L, Han X, Li J, et al. A review on the key issues for lithium-ion battery management in electric vehicles[J]. Journal of Power Sources, 2013, 226：272-288.

[3] Friesen A, Mönnighoff X, Börner M, et al. Influence of temperature on the aging behavior of 18650-type lithium ion cells: A comprehensive approach combining electrochemical characterization and post-mortem analysis[J]. Journal of Power Sources, 2017, 342: 88-97.

[4] Y. Fan, Y. Bao, C. Ling, Y. Chu, X. Tan, S. Yang. Experimental study on the thermal management performance of air cooling for high energy density cylindrical lithium-ion batteries. Applied Thermal Engineering, Volume 155,2019,Pages 96-109.

[5] M. Farag, H. Sweity, M. Fleckenstein, S. Habibi. Combined electrochemical, heat generation, and thermal model for large prismatic lithium-ion batteries in real-time applications, Journal of Power Sources, Volume 360, 2017, Pages 618-633.

[6] Jaewan Kim, Jinwoo Oh, Hoseong Lee, Review on battery thermal management system for electric vehicles, Applied Thermal Engineering, Volume 149, 2019, Pages 192-212.

[7] L. H. Saw, H. M. Poon, H. S. Thiam, Z. Cai, W. T. Chong, N. A. Pambudi, Y. J. King, Novel thermal management system using mist cooling for lithium-ion battery packs, Applied Energy, Volume 223, 2018, Pages 146-158.

[8] Damay N , Forgez C , Bichat M P , et al. Thermal modeling of large prismatic LiFePO4/graphite battery. Coupled thermal and heat generation models for characterization and simulation[J]. Journal of Power Sources, 2015, 283:37-45.

[9] Maryam Ghalkhani, Farid Bahiraei, Gholam-Abbas Nazri, Mehrdad Saif, Electrochemical–Thermal Model of Pouch-type Lithium-ion Batteries, Electrochimica Acta, Volume 247, 2017, Pages 569-587.

[10] Walid Allafi, Cheng Zhang, Kotub Uddin, Daniel Worwood, Truong Quang Dinh, Pedro Ascencio Ormeno, Kang Li, James Marco, A lumped thermal model of lithium-ion battery cells considering radiative heat transfer, Applied Thermal Engineering, Volume 143, 2018, Pages 472-481.

[11] Abada S, Marlair G, Lecocq A, Petit M, Sauvant-Moynot V, Huet F. Safety focused modeling of lithium-ion batteries: a review. J Power Sources 2016;306:178–92.

[12] S. Ma, M. Jiang, P. Tao, C. Song, J. Wu, J. Wang, T. Deng, W. Shang, Temperature effect and thermal impact in lithium-ion batteries: A review, Progress in Natural Science: Materials International, Volume 28, Issue 6, 2018, Pages 653-666.

[13] M. Shadman Rad, D.L. Danilov, M. Baghalha, M. Kazemeini, P.H.L. Notten, Adaptive thermal modeling of Li-ion batteries, Electrochimica Acta,Volume 102, 2013, Pages 183-195.

[14] H. Ruan, J. Jiang, B. Sun, W. Gao, L. Wang, W. Zhang. Online estimation of thermal parameters based on a reduced wide-temperature-range electro-thermal coupled model for lithium-ion batteries. Journal of Power Sources, Volume 396, 2018, pp. 715-724

[15] Armando De Vita, Arpit Maheshwari, Matteo Destro, Massimo Santarelli, Massimiliana Carello. Transient thermal analysis of a lithium-ion battery pack comparing diff erent cooling

solutions for automotive applications. Applied energy, 2017,206,101-112.
[16] Ge H, Aoki T, Ikeda N, Suga S, Isobe T, Li Z, et al. Investigating Lithium Plating in Lithium-Ion Batteries at Low Temperatures Using Electrochemical Model with NMR Assisted Parameterization. J ELECTROCHEM SOC. 2017;164:A1050-A1060
[17] Yang X, Leng Y, Zhang G, Ge S, Wang C. Modeling of lithium plating induced aging of lithium-ion batteries: Transition from linear to nonlinear aging. J POWER SOURCES. 2017;360:28-40
[18] Amiribavandpour P, Shen W, Mu D, Kapoor A. An improved theoretical electrochemical-thermal modelling of lithium-ion battery packs in electric vehicles. J POWER SOURCES. 2015;284:328-338.
[19] Esmaeili J, Jannesari H. Developing heat source term including heat generation at rest condition for Lithium-ion battery pack by up scaling information from cell scale. ENERG CONVERS MANAGE. 2017;139:194-205
[20] Arora S, Shen W, Kapoor A. Neural network based computational model for estimation of heat generation in LiFePO 4 pouch cells of different nominal capacities. COMPUT CHEM ENG. 2017;101:81-94
[21] Chen M, Bai F, Song W, Lv J, Lin S, Feng Z, et al. A multilayer electro-thermal model of pouch battery during normal discharge and internal short circuit process. APPL THERM ENG. 2017;120:506-516.
[22] Modeling of Galvanostatic Charge and Discharge of the Lithium/Polymer/Insertion[C]// Cell", J. Electrochemical Soc. 1993.
[23] Arora P , White R E , Doyle M . Capacity Fade Mechanisms and Side Reactions in Lithium‐Ion Batteries[J]. Cheminform, 2010, 29(47):no-no.
[24] Newman, Bernardi, Pawlikowski. A General Energy-Balance for Battery Systems[J]. Journal of the Electrochemical Society, 1985, 132(1).
[25] Xiao Y , Fahimi B . [IEEE 2014 IEEE Transportation Electrification Conference and Expo (ITEC) - Dearborn, MI (2014.6.15-2014.6.18)] 2014 IEEE Transportation Electrification Conference and Expo (ITEC) - State-space based multi-nodes thermal model for Lithium-ion battery[J]. 2014:1-7.
[26] Tian N , Fang H , Wang Y . 3-D Temperature Field Reconstruction for a Lithium-Ion Battery Pack: A Distributed Kalman Filtering Approach[J]. IEEE Transactions on Control Systems Technology, 2017:1-8.
[27] Xiong R, Tian J, Mu H, Wang C. A systematic model-based degradation behavior recognition and health monitoring method for lithium-ion batteries. APPL ENERG. 2017;207:372-383.
[28] Liu B, Yin S, Xu J. Integrated computation model of lithium-ion battery subject to nail penetration. APPL ENERG. 2016;183:278-289.
[29] Dai H, Xu T, Zhu L, Wei X, Sun Z. Adaptive model parameter identification for large capacity Li-ion batteries on separated time scales. APPL ENERG. 2016;184:119-131
[30] Chalise D, Shah K, Halama T, Komsiyska L, Jain A. An experimentally validated method for temperature prediction during cyclic operation of a Li-ion cell. INT J HEAT MASS TRAN. 2017;112:89-96.
[31] Samba A, Omar N, Gualous H, Capron O, Van den Bossche P, Van Mierlo J. Impact of Tab Location on Large Format Lithium-Ion Pouch Cell Based on Fully Coupled Tree-Dimensional Electrochemical-Thermal Modeling. ELECTROCHIM ACTA.

2014;147:319-329.
[32] Bazinski SJ, Wang X, Sangeorzan BP, Guessous L. Measuring and assessing the effective in-plane thermal conductivity of lithium iron phosphate pouch cells. ENERGY. 2016;114:1085-1092
[33] Richter F, Vie PJS, Kjelstrup S, Burheim OS. Measurements of ageing and thermal conductivity in a secondary NMC-hard carbon Li-ion battery and the impact on internal temperature profiles. ELECTROCHIM ACTA. 2017;250:228-237.
[34] Hannan MA, Lipu MSH, Hussain A, Mohamed A. A review of lithium-ion battery state of charge estimation and management system in electric vehicle applications: Challenges and recommendations. Renewable and Sustainable Energy Reviews. 2017;78:834-854
[35] Werner D , Loges, André, Becker D J , et al. Thermal conductivity of Li-ion batteries and their electrode configurations – A novel combination of modelling and experimental approach[J]. Journal of Power Sources, 2017, 364:72-83.